

## Spatiotemporal dynamics of a buoyancy-driven turbulent fire

Takumi Tokami,<sup>1</sup> Takayoshi Hachijo,<sup>1</sup> Takaya Miyano,<sup>2</sup> and Hiroshi Gotoda<sup>1,\*</sup>

<sup>1</sup>*Department of Mechanical Engineering, Tokyo University of Science, 6-3-1 Nijuku, Katsushika-ku, Tokyo 125-8585, Japan*

<sup>2</sup>*Department of Mechanical Engineering, Ritsumeikan University, 1-1-1 Nojihigashi, Kusatsu, Shiga 525-8577, Japan*



(Received 20 November 2019; accepted 14 March 2020; published 28 April 2020)

We numerically study the spatiotemporal dynamics and predictability of a buoyancy-driven turbulent fire. A significant transition from order to disorder structures can be observed from the mean degree in the spatial horizontal visibility graph. The gravitational term (baroclinic torque term) in the vorticity equation has a significant impact on the formation of the order (disorder) structure in the near field (far field). The entropy flow transport from temperature to flow velocity fluctuations is predominant near the interface between hot combustion products and ambient air. The transfer entropy is an important measure for determining the predictability of flow velocity fluctuations in the near field obtained by reservoir computing.

DOI: [10.1103/PhysRevE.101.042214](https://doi.org/10.1103/PhysRevE.101.042214)

### I. INTRODUCTION

The complex coupling of hydrodynamic convective flow, heat-mass diffusion, and a rapid chemical reaction generates various remarkable flame front instabilities, leading to the emergence of intriguing spatiotemporal chaos during combustion. Buoyancy-driven flame puffing, which is widely observed in fire dynamics, is an important class of flame front instability in diffusion flames. A whole flow field forming open diffusion flames predominately comprises two gases: hot combustion products (low-density gas) behind the flame front and cold ambient air (high-density gas). The buoyancy-driven Kelvin–Helmholtz-type instability destabilizes the interface between the two gases, resulting in the formation and transport of a toroidal vortex [1–3]. The strong interference of the toroidal vortex with the flame front deforms the flame configuration and eventually produces self-sustained flame front oscillations with large amplitudes owing to unstable density stratification, i.e., the Rayleigh–Taylor instability mechanism [4]. These processes significantly contribute to the onset, growth, and development of a buoyancy-driven turbulent fire [5]. Note that the formation of a nonlinear global mode, which originates from a local absolute instability in the near field, plays an important role in the dynamics of flame puffing during a turbulent fire [6–8]. Thus far, many experimental and numerical studies on buoyant plumes and pool fires have revealed the spatial distributions of the instantaneous and time-averaged flow velocity [9–15], vorticity [14,16,17], temperature [4,10–12,14–18], and turbulent statistics [10–12,15,19], including the characterization of the dominant oscillation mode based on the empirical correlation in terms of the Strouhal number, the Froude number, the Richardson number, and the Reynolds number [4,9,17,18,20–25].

Nonlinear time series analysis integrating chaos theory and fractal theory makes it possible to distill the determinism hidden in complex systems and provides an over-

arching understanding and interpretation of the underlying dynamics. It has been widely applied to the dynamic behavior of various flame front instabilities [26–30] and thermoacoustic combustion instabilities [31–40]. However, clarification of the spatiotemporal dynamics of a buoyancy-driven turbulent fire using nonlinear time series analysis still remains uncertain. Our recent numerical computations of a buoyancy-driven turbulent fire [41,42] have shown the formation of two important dynamical states in flow velocity and temperature fluctuations in the near and far fields. The former state is a low-dimensional deterministic chaos state in the near field dominated by the unstable motion of toroidal vortices, whereas the latter state is a high-dimensional chaos state in the far field forming a well-developed turbulent plume. The existence of these dynamical states was clearly shown by the multiscale entropy-causality plane [43] in terms of statistical complexity. We have also demonstrated the suitability of permutation entropy [44] in terms of symbolic dynamics for quantifying the randomness of flow velocity fluctuations, proposing an empirical correlation consisting of the mean permutation entropy and the Froude number [45].

Our main interests in this study are threefold: (i) deeper understanding of the spatiotemporal dynamics during a buoyancy-driven turbulent fire gained from graph networks, (ii) elucidation of the mutual interaction of flow velocity and temperature fluctuations on the basis of information theory, and (iii) prediction of flow velocity fluctuations using machine learning. These points are challenging subjects and have yet to be tackled in the field of fire physics and science. Graph networks consisting of vertexes and edges, which appear in real-world complex systems, are useful for understanding the topological structures in complex spatiotemporal dynamics. We first adopt the spatial horizontal visibility graph [46] for flow velocity fluctuations, and we attempt to clarify the physical link between the mean degree in the networks and the buoyancy-driven terms in the vorticity equation. The transfer entropy [47] incorporating directed information transport enables us to quantify the mutual interactions between two variables. We estimate the transfer entropy for flow velocity

\*Corresponding author: [gotoda@rs.tus.ac.jp](mailto:gotoda@rs.tus.ac.jp)

and temperature fluctuations. Machine learning is becoming a useful method for solving various problems in physics. For example, it has been used as a tool to develop new combustion control technologies [48,49]. Recently, a machine learning called reservoir computing has been introduced, which is a new approach to recurrent neural networks. An effective method of reservoir computing, i.e., echo state networks, has been proposed by Jaeger and coworkers [50–52] and has been applied to nonlinear time series prediction [53–55]. In the final part of this paper, we explore the predictability of flow velocity fluctuations using echo state networks.

This paper comprises four sections. A brief description of the numerical computation and the methodological framework of nonlinear time series analysis is given in Sec. II. We present the numerical results and discussion in Sec. III. A summary is provided in Sec. IV.

## II. NUMERICAL COMPUTATION AND NONLINEAR TIME SERIES ANALYSIS

### A. Numerical computation

In this study, we adopt nonlinear time series analysis for the numerical data of a spatiotemporal structure in a buoyancy-driven turbulent fire obtained by large-eddy simulation [41,42]. Note that the numerical data for 28 s are analyzed after passing the initial transient in the numerical simulation. The governing equations for describing the spatiotemporal structure in the turbulent fire, the discretization method of the governing equations, and the boundary conditions are the same as those in previous studies [41,42]. We consider the mass conservation equation, the momentum conservation equation, the energy conservation equation, and the chemical species equations as the governing equations. The Smagorinsky subgrid-scale model is adopted for the viscous stress in the momentum conservation equation. We also consider a global single-step irreversible chemical reaction, a mixture fraction combustion model, and a low-Mach-number flow. The computational domains in the  $x$ ,  $y$ , and  $z$  directions are set to 2.0, 2.0, and 4.0 m, respectively. Methane gas is supplied from a square center area with dimensions of 1 m  $\times$  1 m.

### B. Nonlinear time series analysis

The horizontal visibility graph proposed by Luque *et al.* [56] serves as a bridge between the dynamical state in time series and networks and has been utilized to treat nonlinear dynamics of various flame front instabilities [29,42] and thermoacoustic combustion instabilities [57–59]. Lacasa and Iacovacci [46] have recently proposed a methodology for constructing a horizontal visibility graph in an instantaneous two-dimensional spatial field. In this study, we focus on the spatial horizontal visibility graph as a possible way of extracting the topological structure hidden in flow velocity fluctuations from the viewpoint of graph networks. The transformation from the spatial data to the networks follows the original horizontal visibility graph algorithm [56]. Two nodes,  $w(x_i, z_i)$  and  $w(x_j, z_j)$ , in the networks are connected by links

if the following geometrical criterion is satisfied:

$$w(x_i, z_i), w(x_j, z_j) > w(x_n, z_n) \quad (i < n < j). \quad (1)$$

Here,  $w(x, z)$  is the streamwise flow velocity on the  $x$ - $z$  plane. Except for the target grid  $i$ , grid  $j$  corresponds to any of the grids along the horizontal, vertical, and diagonal directions in the two-dimensional spatial field. In this study, we estimate the mean degree  $\langle k \rangle$  in the  $x$  direction.

Recurrence plots [60], which are constructed on the basis of distances between all pairs of points in a phase space, are two-dimensional representations suitable for extracting hidden order and disorder pattern structures in the phase space, and capture the dynamical changes to chaos via bifurcations. Thus far, various recurrence plots (e.g., cross recurrence plots and joint recurrence plots) have been proposed, and a comprehensive overview of recurrence plots is given by Marwan *et al.* [61], including recurrence quantification analysis. Recurrence plots incorporating rank-order patterns in time series on the basis of Bandt and Pompe's concept [44], referred to as symbolic recurrence plots (SRPs), are very useful for dealing with the similarity of two dynamical states in relation to synchronization phenomena [62]. We examine the similarity of flow velocity and temperature fluctuations using SRPs. The adjacency matrix of SRPs consisting of  $R_{ij}$  is obtained as

$$R_{ij} = \begin{cases} 1 & \pi_{w'}^D(t_i) = \pi_{T'}^D(t_j), \\ 0 & \text{otherwise.} \end{cases} \quad (2)$$

Here,  $\pi_{w'}^D(t_i)$  [ $\pi_{T'}^D(t_j)$ ] denotes the rank-order patterns of  $w'$  ( $T'$ ) and  $D$  is the embedding dimension. In this study, we estimate the recurrence rate  $S_{RR}$  representing the density on the diagonal in SRPs:

$$S_{RR} = \frac{1}{N - (D - 1) - |\tau|} \sum_{i=1}^{N-(D-1)-|\tau|} R_{ij}, \quad (3)$$

where  $j$  is set to  $i + \tau$  for the estimation of  $S_{RR}$  in the diagonal direction.  $S_{RR}$  starts to increase as  $w'$  and  $T'$  reach similar dynamical states.

The transfer entropy proposed by Schreiber [47] is a useful measure for quantifying the directed information flow between two variables in spatially extended systems. We estimate the transfer entropy to clarify the mutual interaction of flow velocity and temperature fluctuations. The quantity of information flowing from  $T'$  to  $w'$  with time delay  $\tau$ , denoted as  $S_{E, T' \rightarrow w'}$ , is defined as Eq. (4) using the Kullback–Leibler divergence:

$$S_{E, T' \rightarrow w'} = \sum_{i=1}^{N-\tau} p[w'(t_{i+\tau}), \mathbf{w}_i^k, \mathbf{T}_i^l] \log \frac{p[w'(t_{i+\tau}) | \mathbf{w}_i^k, \mathbf{T}_i^l]}{p[w'(t_{i+\tau}) | \mathbf{w}_i^k]}, \quad (4)$$

where  $S_{E, T' \rightarrow w'}$  ( $S_{E, w' \rightarrow T'}$ ) is the transfer entropy in the direction from  $T'$  to  $w'$  ( $w'$  to  $T'$ );  $\mathbf{w}_i^k = [w'(t_i), w'(t_{i-1}), \dots, w'(t_{i-k+1})]$  and  $\mathbf{T}_i^l = [T'(t_i), T'(t_{i-1}), \dots, T'(t_{i-l+1})]$ ;  $p[w'(t_{i+\tau}), \mathbf{w}_i^k, \mathbf{T}_i^l]$  is the joint probability of  $w'(t_{i+\tau})$ ,  $\mathbf{w}_i^k$ , and  $\mathbf{T}_i^l$ ; and  $p[w'(t_{i+\tau}) | \mathbf{w}_i^k]$  is the conditional probability of  $w'(t_{i+\tau})$  given  $\mathbf{w}_i^k$ . As in a previous study [63],

we set  $k = l = 1$  and  $\tau = 1$ .  $p[w'(t_{i+1}), \mathbf{w}_i^k, \mathbf{T}_i^l]$  is expressed by the joint probability using the kernel estimation [47]:

$$p[w'(t_{i+1}), w'(t_i), T'(t_i)] = \frac{1}{N-1} \sum_{i'=1}^{N-1} \Theta \left[ r - \begin{vmatrix} w'(t_{i'+1}) - w'(t_{i+1}) \\ w'(t_{i'}) - w'(t_i) \\ T'(t_{i'}) - T'(t_i) \end{vmatrix} \right], \quad (5)$$

$$\Theta(z) = \begin{cases} 1 & (z \geq 0), \\ 0 & (z < 0). \end{cases} \quad (6)$$

Here,  $\Theta$  is the Heaviside function.

Reservoir computing has recently attracted much attention as a sophisticated and promising model-free predictor [54]. We introduce reservoir computing with the aim of predicting complex streamwise flow velocity fluctuations. A reservoir computer consists of three layers: an input layer, a reservoir, and an output layer. We employ echo state networks as the simplest form of the reservoir, and we update the reservoir state  $\mathbf{r}(t_i)$  during the training phase of the reservoir computer using

$$\mathbf{r}(t_i + \Delta t) = (1 - \alpha)\mathbf{r}(t_i) + \alpha \tanh[\mathbf{W}\mathbf{r}(t_i) + \mathbf{W}_{\text{in}}\mathbf{u}(t_i)]. \quad (7)$$

Here,  $\mathbf{u}(t_i)$  is the input vector,  $\mathbf{W}_{\text{in}}$  is the weighted matrix between the input layer and the reservoir, and  $\mathbf{W}$  is the  $D_r \times D_r$  adjacency matrix of the reservoir network. The initial states of the weighted matrix are given by a random matrix. The matrix elements of  $\mathbf{W}$  range from  $-1$  to  $1$  subject to a uniform distribution, and  $D_r$  is set to 1000.  $\mathbf{W}$  includes a sparse random matrix with 200 000 nonzero components.  $\alpha$  is the leakage rate corresponding to the update speed of the reservoir dynamics and is varied from zero to unity [64]. After updating the reservoir, the output vector  $\mathbf{v}(t_i)$  is obtained by linear mapping of  $\mathbf{r}$  and  $\mathbf{u}$ :

$$\mathbf{v}(t_i) = \mathbf{W}_{\text{out}} \begin{pmatrix} \mathbf{u}(t_i) \\ \mathbf{r}(t_i) \end{pmatrix}. \quad (8)$$

Here,  $\mathbf{W}_{\text{out}}$  is the weighted matrix between the output layer and the reservoir. This process is repeated for the learning steps, where  $0 \leq i \leq n$ . Tikhonov–Arsenin regularization [65] is employed to optimize  $\mathbf{W}_{\text{out}}$  so as to minimize the error between  $\mathbf{v}(t_i)$  and the training data  $\mathbf{v}_d(t_i)$ :

$$\widehat{\mathbf{W}}_{\text{out}} = \mathbf{v}_d \mathbf{s}^T (\mathbf{s} \mathbf{s}^T + \beta \mathbf{I})^{-1}. \quad (9)$$

Here,  $\mathbf{s}$  is the matrix that is represented as follows:

$$\mathbf{s} = \begin{pmatrix} \mathbf{u}(t_0) & \mathbf{u}(t_0 + \Delta t) & \cdots & \mathbf{u}(t_n) \\ \mathbf{r}(t_0) & \mathbf{r}(t_0 + \Delta t) & \cdots & \mathbf{r}(t_n) \end{pmatrix}. \quad (10)$$

$\beta$  is a regularization coefficient and  $\mathbf{I}$  is the identity matrix. We set  $\mathbf{u}(t_i) = [b; T'(t_i); w'(t_i)]$ ,  $\mathbf{v}_d(t_i) = [T'(t_i + \Delta t); w'(t_i + \Delta t)]$ , and  $\beta = 1 \times 10^{-6}$ . In accordance with a recent study [66], we adopt  $\mathbf{u}(t_i) = [b; T'(t_i); w'_{\text{predict}}(t_i)]$  for the prediction steps, and we finally obtain  $\mathbf{v}(t_i) = [T'_{\text{predict}}(t_i + \Delta t); w'_{\text{predict}}(t_i + \Delta t)]$ . Note that, as in Ref. [66],  $b$  is set to unity.

### III. RESULTS AND DISCUSSION

Figure 1 shows the temporal evolution of the mean degree  $\langle k \rangle$  in the spatial horizontal visibility graph.  $\langle k \rangle$  periodically

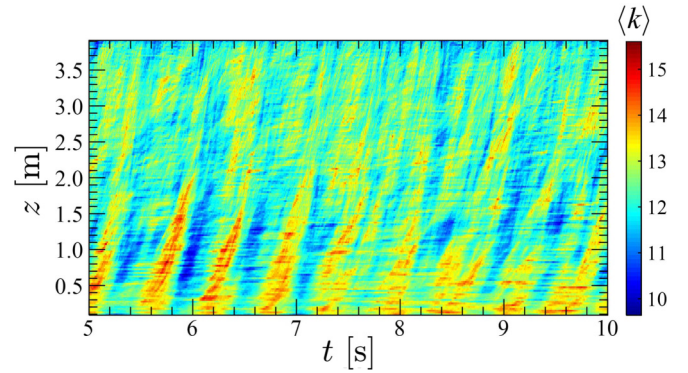


FIG. 1. Temporal evolution of the mean degree  $\langle k \rangle$  in the spatial horizontal visibility graph.

fluctuates with a frequency of approximately 2 Hz at  $z \sim 0.5$  m corresponding to the near field, accompanying the emergence of the primary hub in the networks. Unstable toroidal vortex rings are periodically produced in the continuous flame zone in the near field owing to the buoyancy-driven hydrodynamic shear layer instability between the hot combustion products and the cold surrounding air [41]. The dominant frequency of  $\langle k \rangle$  corresponds to that of the unstable vortex rings. This indicates that the appearance of the order structure in  $\langle k \rangle$  can be attributed to the formation of the unstable vortex rings. As the unstable vortex rings travel downstream owing to the upward buoyant force, they become significantly distorted and break down into vortices with various scales and strengths in an intermittent luminous zone [5], leading to the loss of the periodic structure in  $\langle k \rangle$ . The coalescence and breakdown of the vortices aperiodically occur in the far field forming a fully developed turbulent plume [41]. The periodic structure in  $\langle k \rangle$  vanishes at  $z \sim 3.0$  m, corresponding to the far field. The complex and strong vortex interaction in the far field generates irregularity in the links in the networks, resulting in the appearance of the disorder structure in  $\langle k \rangle$ . The important point to emphasize here is that the buoyancy-driven hydrodynamic shear layer instability and the subsequent Rayleigh–Taylor instability give rise to an interesting transition from an order to disorder structure in the links in the networks constructed from streamwise flow velocity fluctuations. These results also show that the mean degree in the spatial horizontal visibility graph is a useful network measure for understanding the subtle dynamic behavior of a turbulent fire.

The vorticity transport gives us a physical understanding and interpretation of the dynamics of vortical structures during buoyant jet diffusion flames, and its importance has been numerically studied using the vorticity equation [67]. We here discuss the order and disorder structures in the mean degree in the networks during a buoyancy-driven turbulent fire by examining the vorticity transport using the following vorticity equation:

$$\frac{D\boldsymbol{\omega}}{Dt} = (\boldsymbol{\omega} \cdot \nabla)\mathbf{v} - \boldsymbol{\omega}(\nabla \cdot \mathbf{v}) + \frac{1}{\rho^2}(\nabla \rho \times \nabla p) + \frac{1}{\rho^2} \frac{\rho_a}{F_r} (\nabla \rho \times \mathbf{g}) + \nabla \times \left( \frac{1}{\rho} \nabla \cdot \boldsymbol{\tau} \right). \quad (11)$$

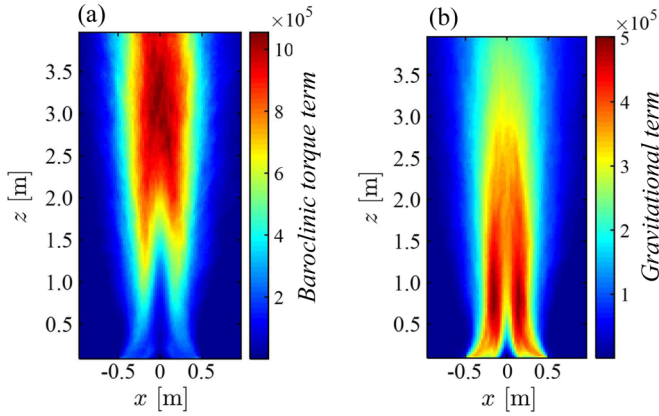


FIG. 2. Spatial distribution of mean values of (a) the baroclinic torque term and (b) the gravitational term estimated from the cross-streamwise vorticity.

Here,  $\omega$  is the vorticity field,  $\mathbf{v}$  is the flow velocity field,  $p$  is the pressure,  $\rho$  is the density,  $\rho_a$  is the density of the ambient air,  $\mathbf{g}$  is the gravity vector,  $\boldsymbol{\tau}$  is the shear stress, and  $F_r$  is the Froude number. A toroidal vortex ring (spiral vortex) contains the cross-streamwise  $x$  and  $y$  components (streamwise  $z$  component) of the vorticity. The right-hand side of Eq. (11) includes two important vortex production terms driven by the density gradient: the baroclinic torque term  $[= (1/\rho^2)(\nabla\rho \times \nabla p)]$  and the gravitational term  $[= \rho_a/(\rho^2 F_r)(\nabla\rho \times \mathbf{g})]$ . These terms determine the promotion of buoyancy-dominated flow vorticity. On this basis, we focus on the baroclinic torque and gravitational terms in this study. Figure 2 shows the spatial distribution of the mean values of the baroclinic torque and gravitational terms estimated from the cross-streamwise vorticity. The gravitational term takes high values in the continuous flame zone and the intermittent luminous zone, particularly in the near field forming the unstable toroidal vortex rings. The interaction of the density gradient and gravity dominates the generation of the vorticity in the near field. The magnitude of the gravitational term decreases in the far field, indicating a decrease in vorticity generation. As shown in Fig. 1, a periodic structure of  $\langle k \rangle$  emerges in the near field and becomes lost in the far field. This means that the gravitational term is the significant source for the periodic formation of the mean degree in the networks. In contrast, the magnitude of the baroclinic torque term significantly increases as the periodic structure of  $\langle k \rangle$  begins to collapse, and takes high values in the far field. The baroclinic torque term plays an important role in the aperiodic formation of the mean degree in the networks during a buoyancy-driven turbulent fire.

Figure 3 shows the variation in  $S_{RR}$  as a function of  $\tau_a$  for different  $z$ . Note that  $\tau_a$  corresponds to the actual delay time ( $=\tau\Delta t$ , where  $\Delta t$  is the time resolution of flow velocity and temperature fluctuations).  $S_{RR}$  takes high values at  $z \sim 0.5$  m, indicating that the temperature and flow velocity fluctuations are synchronized with each other. It periodically changes in terms of  $\tau_a$  in the near field, indicating the presence of in-phase and antiphase states between the two fluctuations. Above the intermittent luminous zone,  $S_{RR}$  significantly decreases with increasing  $z$  and reaches approximately 0.28 in

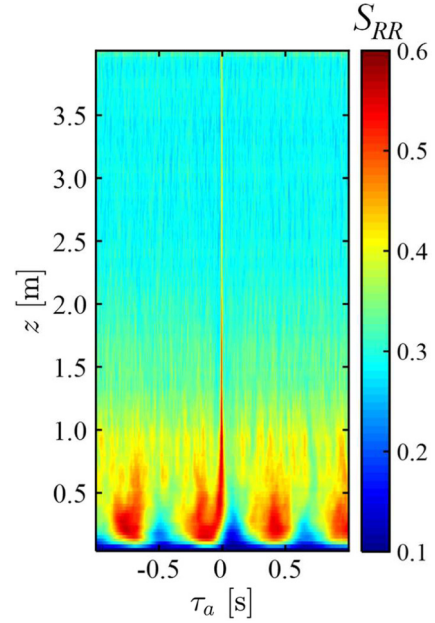


FIG. 3. Variation in the symbolic recurrence rate  $S_{RR}$  as a function of delay time  $\tau_a$  for different  $z$ .

a wide range of  $\tau_a$  at  $z \geq 2.5$  m. We previously reported that the randomness of flow velocity and temperature fluctuations is high in the far field owing to the formation of high-dimensional chaos [41,42]. On this basis, it is conceivable that the flow velocity and temperature fluctuations in the far field are not synchronized with each other. The spatial distribution of  $\Delta S_E$   $[= \Delta S_{E,T' \rightarrow w'} - \Delta S_{E,w' \rightarrow T'}]$  is shown in Fig. 4. We clearly observe that except for the region near the centerline of the fire source,  $\Delta S_E$  takes significantly high positive values near the shear layer region between hot combustion products and ambient air. The entropy transfer from the combustion-driven temperature to buoyancy-driven flow velocity fluctua-

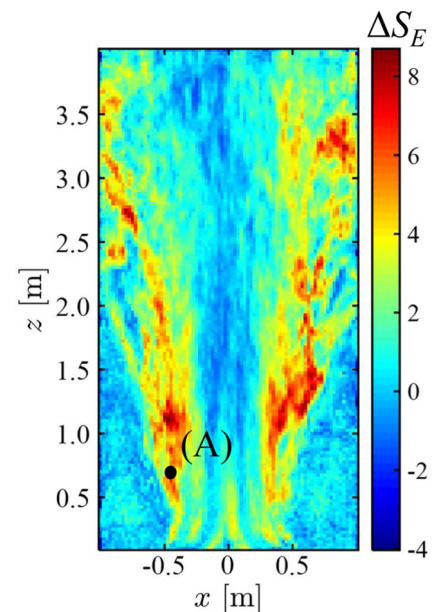


FIG. 4. Spatial distribution of the entropy difference  $\Delta S_E$ .

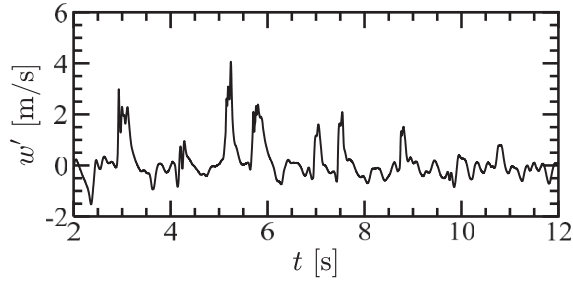


FIG. 5. Temporal evolution of the streamwise flow velocity fluctuations  $w'$  extracted from region (A) with a high entropy difference  $\Delta S_E$ .

tions is predominant in this region. Many previous studies on the dynamics of flame flickering and puffing fires [1–4,10–16,18–21,23,24] did not reveal the directional dependence between flow velocity and temperature fields. The direction of the mutual interaction between two physical quantities has recently been studied by one of the authors [63] for a different system using the transfer entropy. The transfer entropy has potential use in extracting the driving region of a turbulent fire, in the sense that it considers the direction of the mutual interaction between flow velocity and temperature fluctuations.

Figure 5 shows the temporal evolution of  $w'$  extracted from the high- $\Delta S_E$  region (A) (see Fig. 4). Intermittent behavior clearly appears in streamwise flow velocity fluctuations. Intermittent phenomena that suddenly alternate between two dynamical states are of much interest in current nonlinear science and physics. Intermittency is mainly classified into various types including Pomeau–Manneville intermittency types I, II, and III [68], crisis-induced intermittency [69], and on-off intermittency [70–73]. Some types can appear in hydrodynamical systems. In fact, irregularly distributed turbulent bursts and laminar phases alternately appear in a Lorenz system describing the global dynamics of Rayleigh–Benard convection [74] as one of the representative intermittent phenomena. On-off intermittency can be generally characterized by power-law scaling with a universal exponent of  $-3/2$  in the probability distribution of laminar phase duration and has relatively recently been discovered in a turbulent Couette flow [75] and mercury flow in a heated pipe [76]. In this study, we consider the small-amplitude fluctuations in  $w'$  as the laminar phase to estimate the probability distribution. Figure 6 shows the probability distribution  $P(t_d)$  of the time intervals  $t_d$  exhibiting small-amplitude fluctuations. Note that  $t_d$  is estimated similarly to that in Refs. [77,78]. The threshold of the discriminant function [78] is set to  $10 \text{ m/s}^2$  in this study.  $P(t_d)$  has a clear scaling power law with  $\gamma = -3/2$ , indicating the possible presence of on-off intermittency, where  $\gamma$  is the scaling exponent. Irregular alternation between turbulent and nonturbulent regimes occurs in the flow velocity fluctuations in a turbulent jet and wake, which accompany bulges and indentations of the interface [79]. This irregular alternating motion exhibits intermittency.  $w'$  exhibits behavior similar to that in Ref. [79]. Although our physical setting is different from that in Ref. [79], the irregular alternation between turbulent combustion products and nonturbulent ambient air may

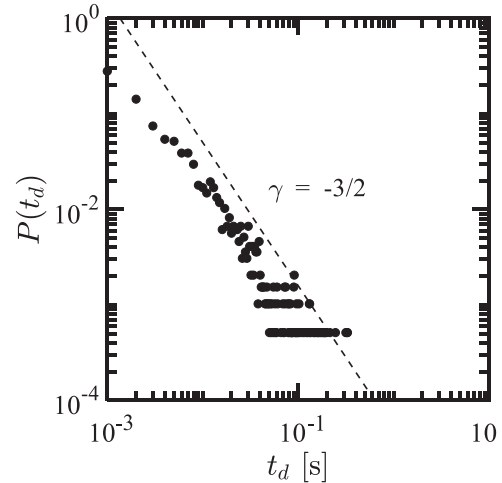


FIG. 6. Probability distribution  $P(t_d)$  of the time intervals  $t_d$  exhibiting small-amplitude fluctuations.

be related to the onset of temporal on-off intermittency in  $w'$ . Note that on-off intermittency also occurs in the high- $\Delta S_E$  region in the far field.

Figure 7 shows the variation in the correlation coefficient  $C$  between the predicted values and the corresponding reference values of  $w'$  as a function of  $x$  for different  $z$ . Two peaks with high  $C$  ( $\sim 0.75$ ) are observed at  $z = 0.7 \text{ m}$ , showing the high predictability of flow velocity fluctuations. The  $x$ - $z$  locations where these two peaks appear correspond reasonably well to the formation region of the intermittent flow

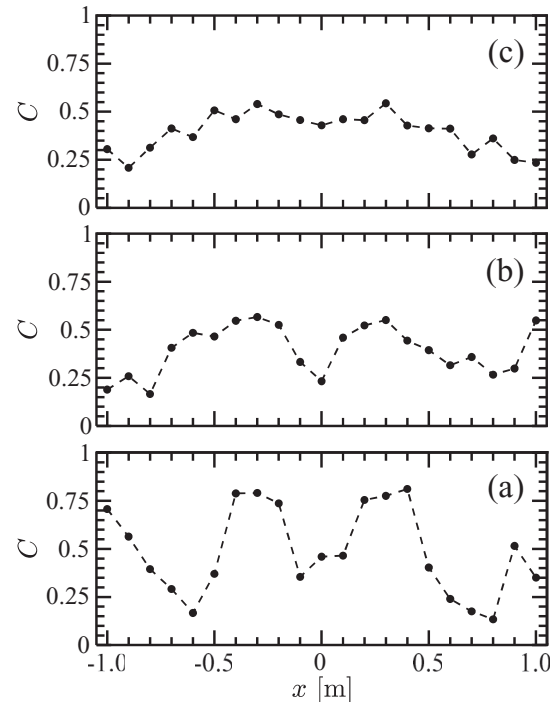


FIG. 7. Variation in the correlation coefficient  $C$  between the predicted values and the corresponding reference values of streamwise flow velocity fluctuations  $w'$  as a function of  $x$  for different  $z$ . (a)  $z = 0.7 \text{ m}$ , (b)  $z = 2.0 \text{ m}$ , and (c)  $z = 3.0 \text{ m}$ .

velocity fluctuations. The results shown in Figs. 4 and 5 indicate that the high predictability in the near field is strongly associated with high entropy transfer from temperature to flow velocity fluctuations. At  $z = 3.0$  m, the two peaks disappear and  $C$  reaches approximately 0.4. The irregularity of the streamwise flow velocity fluctuations significantly increases at  $z = 3.0$  m owing to the coalescence and breakdown of vortices with various scales and strengths. This results in the disappearance of the twin peaks in the distribution of  $C$ . In other words, the formation of high-dimensional chaos [41] causes a significant decrease in the predictability in the far field. Turbulent flow exhibits multiscale and multifractal structures in the spatiotemporal flow velocity fluctuations. They are important characteristics of high-dimensional chaos. In our previous study [41], the exponential sensitivity to initial conditions, i.e., the orbital instability, was investigated using the scale-dependent Lyapunov exponent method [80], whereas the multifractal structure has not been explored. In this study, we provide an additional result on the fractality in  $w'$  using the detrended-fluctuation analysis-based multifractal formulation [81]. Figure 8 shows the  $q$ th-order statistical moment  $F(q, s)$  as a function of  $s$  at  $q = 2$ , together with the singularity spectrum  $f(\alpha)$  at  $z = 3.0$  m.  $F(q, s)$  is estimated as

$$F(q, s) = \left\{ \frac{1}{N_s} \sum_{v=1}^{N_s} [F^2(s, v)]^{q/2} \right\}^{1/q}, \quad (12)$$

$$F^2(s, v) = \frac{1}{s} \sum_{i=1}^s [w'_{cs}(t_{(v-1)s+i}) - w'_v(t_{(v-1)s+i})]^2, \quad (13)$$

where  $w'_{cs}(t) = \sum_{k=1}^i w'(t_k)$ ,  $s$  is the length of the segment, and  $w'_v(t)$  is the fitting polynomial in the segment. After  $F(q, s)$  is scaled with  $s^H$ ,  $f(\alpha)$  is obtained by the Legendre transformation:

$$f(\alpha) = q(\alpha - H) + 1, \quad (14)$$

where  $\alpha$  is the singularity strength. The  $\log_2 F(q, s)$  versus  $\log_2 s$  plot exhibits a linear correlation with a clear scaling law. A unimodal and downward concave is formed by the curve of  $f(\alpha)$ . This clearly shows the presence of a multifractal structure exhibiting various self-similarities in the far field. The variation in  $\Delta S_E$  as a function of  $x$  for different  $z$  is shown in Fig. 9. The distributions of  $\Delta S_E$  in terms of  $x$  in the near field correspond reasonably well to those of  $C$  shown in Fig. 7. This result clearly shows that the entropy transfer from temperature to flow velocity fluctuations plays an important role in the predictability of flow velocity fluctuations in the near field. The transfer entropy is an important measure for determining the predictability of flow velocity fluctuations in the near field obtained by reservoir computing. A low-dimensional Lorenz system with 3 degrees of freedom is widely used to explain nonlinear dynamical mechanisms appearing in buoyancy-driven irregular convective flows. A recent numerical study [66] on reservoir computing reported that the short-term prediction of  $X$  is feasible by using  $Y$  in the Lorenz equation, where  $X$  ( $Y$ ) corresponds to the flow convective strength (temperature fluctuations). The low-dimensional deterministic chaos produced by the Lorenz equation does not represent the spatiotemporal dynamics of flow velocity in this

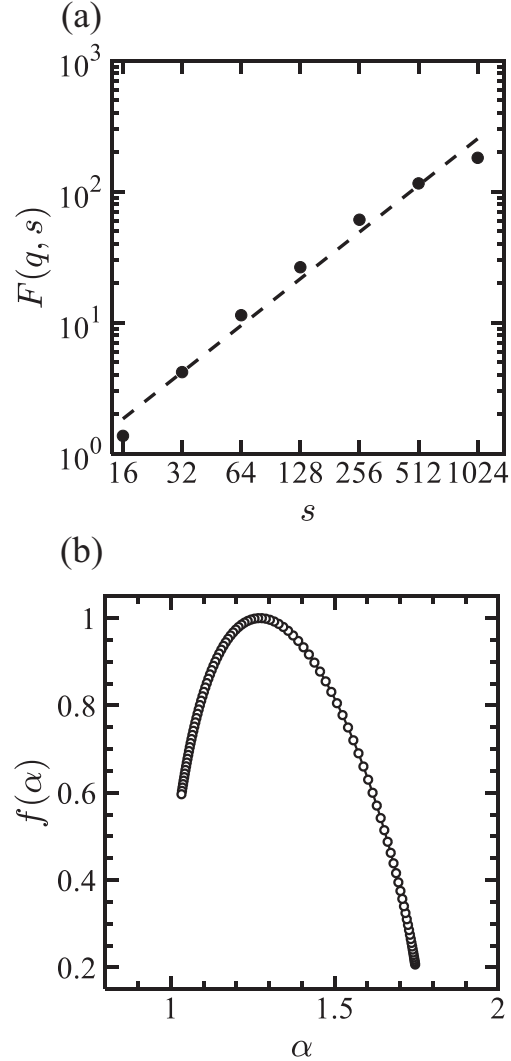


FIG. 8. (a) Variation in the  $q$ th-order statistical moment  $F(q, s)$  as a function of  $s$  at  $q = 2$ , together with (b) the singularity spectrum  $f(\alpha)$  at  $z = 3.0$  m.

study, but the finding by Weng *et al.* [66] sufficiently supports our result of the predictability of flow velocity fluctuations in the near field. In an echo state network, sparsely coupled reservoir nodes, the activating functions of which are usually given as hyperbolic tangent or sigmoid functions, form a recurrent network that generates evanescent library patterns with long short-term memory in response to current input data. Predictions are made at the output node as the weighted sum of the library patterns. Once the weight coefficients for coupling the input and reservoir nodes and those between reservoir nodes have been appropriately determined irrespective of learning examples, the weight coefficients for coupling the reservoir and the output nodes to generate the superposition of the library patterns are optimized using a supervised learning algorithm. In this sense, reservoir computing can be said to be a promising simulator of chaotic dynamics.

In this work, we carried out a numerical study to clarify the nonlinear dynamics of a buoyancy-driven turbulent fire on the basis of graph networks and information theory,

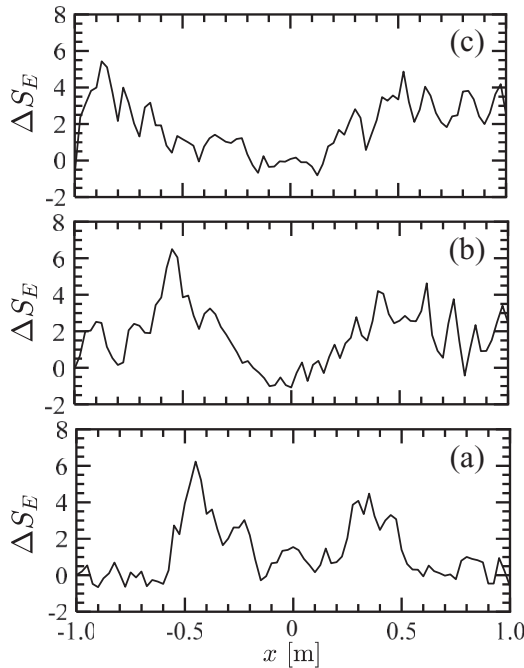


FIG. 9. Variation in the entropy difference  $\Delta S_E$  as a function of  $x$  for different  $z$ . (a)  $z = 0.7$  m, (b)  $z = 2.0$  m, and (c)  $z = 3.0$  m.

including the prediction of the dynamics by a machine-learning approach. The most interesting and important findings in this study are the following.

(i) The gravitational term (baroclinic torque term) in the vorticity equation has a significant impact on the formation of order (disorder) patterns in the mean degree in the spatial visibility graph.

(ii) The directional entropy transfer from temperature to flow velocity fluctuations is predominant near the shear layer between hot combustion products and ambient air.

(iii) The transfer entropy is significantly related to the predictability of flow velocity fluctuations in the near field obtained by reservoir computing.

To the best of our knowledge, these points have not yet been clarified in the treatment of a buoyancy-driven turbulent fire. Our results are expected to provide a deeper understanding and interpretation of nonlinear dynamics in a turbulent fire.

#### IV. SUMMARY

We have numerically studied the spatiotemporal dynamics of a buoyancy-driven turbulent fire on the basis of graph networks and information entropy, including the predictability of the dynamics by the machine-learning approach. A significant transition from order to disorder structures can be observed from the mean degree in the spatial horizontal visibility graph constructed from the streamwise flow velocity fluctuations. The order structure is formed in the near field dominated by the unstable motion of toroidal vortex rings, whereas the disorder structure is formed in the far field exhibiting high-dimensional deterministic chaos. The gravitational term (baroclinic torque term) in the vorticity equation has a significant impact on the formation of the order (disorder) structure in the near field (far field). The directional entropy flow transport from the combustion-driven temperature to the buoyancy-driven turbulent velocity field, which is quantified by the transfer entropy, is predominant near the interface between hot combustion products and ambient air. Reservoir computing enables the prediction of the intermittent flow velocity fluctuations in the near field. The transfer entropy is an important measure for determining the predictability of flow velocity fluctuations in the near field obtained by reservoir computing.

#### ACKNOWLEDGMENTS

This research is partially supported by the Private University Research Branding Project (2017–2021) from the Ministry of Education, Culture, Sports, Science and Technology. We thank Mr. Kentaro Kubota (Tokyo University of Science) for his support with the computations on the spatial horizontal visibility graph.

- 
- [1] L. D. Chen, J. P. Seaba, W. M. Roquemore, and L. P. Goss, *Proc. Combust. Inst.* **22**, 677 (1989).
- [2] V. R. Katta and W. M. Roquemore, *Combust. Flame* **92**, 274 (1993).
- [3] H. Gotoda, S. Kawaguchi, and Y. Saso, *Exp. Therm. Fluid Sci.* **32**, 1759 (2008).
- [4] A. F. Ghoniem, I. Lakkis, and M. Soteriou, *Proc. Combust. Inst.* **26**, 1531 (1996).
- [5] D. Drysdale, *An Introduction to Fire Dynamics* (Wiley, New York, 1994).
- [6] A. Lingens, M. Reeker, and M. Schreiber, *Exp. Fluids* **20**, 241 (1996).
- [7] K. H. Luo, *Eur. J. Mech. B/Fluids* **23**, 443 (2004).
- [8] M. P. Juniper, L. K. B. Li, and J. W. Nicholas, *Proc. Combust. Inst.* **32**, 1191 (2009).
- [9] B. M. Cetegen and K. D. Kasper, *Phys. Fluids* **8**, 2974 (1996).
- [10] E. J. Weckman and A. B. Strong, *Combust. Flame* **105**, 245 (1996).
- [11] S. R. Tieszen, T. J. O'Hern, R. W. Schefer, E. J. Weckman, and T. K. Blanchat, *Combust. Flame* **129**, 378 (2002).
- [12] S. R. Tieszen, T. J. O'Hern, E. J. Weckman, and R. W. Schefer, *Combust. Flame* **139**, 126 (2004).
- [13] P. E. DesJardin, T. J. O'Hern, and S. R. Tieszen, *Phys. Fluids* **16**, 1866 (2004).
- [14] Y. Xin, J. P. Gore, K. B. McGrattan, R. G. Rehm, and H. R. Baum, *Combust. Flame* **141**, 329 (2005).
- [15] Y. Xin, S. A. Filatyev, K. Biswas, J. P. Gore, R. G. Rehm, and H. R. Baum, *Combust. Flame* **153**, 499 (2008).
- [16] R. W. Davis, E. F. Moore, W. M. Roquemore, L. D. Chen, V. Vilimpoc, and L. P. Goss, *Combust. Flame* **83**, 263 (1991).
- [17] H. Sato, G. Kushida, K. Amagai, and M. Arai, *Proc. Combust. Inst.* **29**, 1671 (2002).

- [18] W. E. Mell, K. B. McGrattan, and H. R. Baum, *Proc. Combust. Inst.* **26**, 1523 (1996).
- [19] X. Zhou, K. H. Luo, and J. J. R. Williams, *Combust. Flame* **129**, 11 (2002).
- [20] A. Hamins, J. C. Yang, and T. Kashiwagi, *Proc. Combust. Inst.* **24**, 1695 (1992).
- [21] B. M. Cetegen and T. A. Ahmed, *Combust. Flame* **93**, 157 (1993).
- [22] B. M. Cetegen, Y. Dong, and M. C. Soteriou, *Phys. Fluids* **10**, 1658 (1998).
- [23] B. M. Cetegen and Y. Dong, *Exp. Fluids* **28**, 546 (2000).
- [24] L. Hu, J. Hu, and J. L. de Ris, *Combust. Flame* **162**, 1095 (2015).
- [25] H. Abe, A. Ito, and H. Torikai, *Proc. Combust. Inst.* **35**, 2581 (2015).
- [26] H. Gotoda, T. Miyano, and I. G. Shepherd, *Phys. Rev. E* **81**, 026211 (2010).
- [27] H. Gotoda, T. Ikawa, K. Maki, and T. Miyano, *Chaos* **22**, 033106 (2012).
- [28] L. K. B. Li and M. P. Juniper, *Proc. Combust. Inst.* **34**, 947 (2013).
- [29] H. Kinugawa, K. Ueda, and H. Gotoda, *Chaos* **26**, 033104 (2016).
- [30] H. Gotoda, H. Kobayashi, and K. Hayashi, *Phys. Rev. E* **95**, 022201 (2017).
- [31] L. Kabiraj, A. Saurabh, P. Wahi, and R. I. Sujith, *Chaos* **22**, 023129 (2012).
- [32] V. Nair and R. I. Sujith, *Chaos* **23**, 033136 (2013).
- [33] V. Nair, G. Thampi, and R. I. Sujith, *J. Fluid Mech.* **756**, 470 (2014).
- [34] K. Kashinath, I. C. Waugh, and M. P. Juniper, *J. Fluid Mech.* **761**, 399 (2014).
- [35] H. Gotoda, Y. Okuno, K. Hayashi, and S. Tachibana, *Phys. Rev. E* **92**, 052906 (2015).
- [36] L. Kabiraj, A. Saurabh, N. Karimi, A. Sailor, E. Mastorakos, A. P. Dowling, and C. O. Paschereit, *Chaos* **25**, 023101 (2015).
- [37] S. Balusamy, L. K. B. Li, Z. Han, M. P. Juniper, and S. Hochgreb, *Proc. Combust. Inst.* **35**, 3229 (2015).
- [38] J. Tony, E. A. Gopalakrishnan, E. Sreelekha, and R. I. Sujith, *Phys. Rev. E* **92**, 062902 (2015).
- [39] S. Suresha, R. I. Sujith, B. Emerson, and T. Lieuwen, *Phys. Rev. E* **94**, 042206 (2016).
- [40] R. Sampath, M. Mathur, and S. R. Chakravarthy, *Phys. Rev. E* **94**, 062209 (2016).
- [41] K. Takagi, H. Gotoda, I. T. Tokuda, and T. Miyano, *Phys. Rev. E* **96**, 052223 (2017).
- [42] K. Takagi, H. Gotoda, I. T. Tokuda, and T. Miyano, *Phys. Lett. A* **382**, 3181 (2018).
- [43] L. Zunino, M. C. Soriano, and O. A. Rosso, *Phys. Rev. E* **86**, 046210 (2012).
- [44] C. Bandt and B. Pompe, *Phys. Rev. Lett.* **88**, 174102 (2002).
- [45] K. Takagi and H. Gotoda, *Phys. Rev. E* **98**, 032207 (2018).
- [46] L. Lacasa and J. Iacovacci, *Phys. Rev. E* **96**, 012318 (2017).
- [47] T. Schreiber, *Phys. Rev. Lett.* **85**, 461 (2000).
- [48] T. Kobayashi, S. Murayama, T. Hachijo, and H. Gotoda, *Phys. Rev. Appl.* **11**, 064034 (2019).
- [49] T. Hachijo, S. Masuda, T. Kurosaka, and H. Gotoda, *Chaos* **29**, 103123 (2019).
- [50] H. Jaeger, German National Research Center for Information Technology GMD Report No. 148, 2001.
- [51] H. Jaeger, M. Lukosevicius, D. Popovici, and U. Siewert, *Neural Networks* **20**, 335 (2007).
- [52] M. Lukosevicius and H. Jaeger, *Comput. Sci. Rev.* **3**, 127 (2009).
- [53] J. Pathak, Z. Lu, B. R. Hunt, M. Girvan, and E. Ott, *Chaos* **27**, 121102 (2017).
- [54] J. Pathak, B. Hunt, M. Girvan, Z. X. Lu, and E. Ott, *Phys. Rev. Lett.* **120**, 024102 (2018).
- [55] A. Shinozaki, K. Shiozawa, K. Kajita, T. Miyano, and Y. Horio, in *2019 International Joint Conference on Neural Networks*, Paper N-20022, 2019.
- [56] B. Luque, L. Lacasa, F. J. Ballesteros, and A. Robledo, *Chaos* **22**, 013109 (2012).
- [57] M. Murugesan and R. I. Sujith, *J. Fluid Mech.* **772**, 225 (2015).
- [58] H. Gotoda, H. Kinugawa, R. Tsujimoto, S. Domen, and Y. Okuno, *Phys. Rev. Appl.* **7**, 044027 (2017).
- [59] Y. Guan, L. K. B. Li, B. Ahn, and K. T. Kim, *Chaos* **29**, 053124 (2019).
- [60] J. Eckmann, S. O. Kamphorst, and D. Ruelle, *Europhys. Lett.* **4**, 973 (1987).
- [61] N. Marwan, M. C. Romano, M. Thiel, and J. Kurths, *Phys. Rep.* **438**, 237 (2007).
- [62] A. Groth, *Phys. Rev. E* **72**, 046220 (2005).
- [63] T. Hashimoto, H. Shibuya, H. Gotoda, Y. Ohmichi, and S. Matsuyama, *Phys. Rev. E* **99**, 032208 (2019).
- [64] M. Lukosevicius, *Neural Networks: Tricks of the Trade*, Lecture Notes in Computer Science Vol. 659 (Springer, New York, 2012).
- [65] A. N. Tikhonov and V. Y. Arsenin, *Solutions of Ill-Posed Problems* (Winston & Sons, Washington, D.C., 1977).
- [66] T. Weng, H. Yang, C. Gu, J. Zhang, and M. Small, *Phys. Rev. E* **99**, 042203 (2019).
- [67] X. Jiang and K. H. Luo, *Combust. Flame* **133**, 29 (2003).
- [68] P. Manneville and Y. Pomeau, *Phys. Lett. A* **75**, 1 (1979).
- [69] C. Grebogi, E. Ott, F. Romeiras, and J. A. Yorke, *Phys. Rev. A* **36**, 5365 (1987).
- [70] N. Platt, E. A. Spiegel, and C. Tresser, *Phys. Rev. Lett.* **70**, 279 (1993).
- [71] J. F. Heagy, N. Platt, and S. M. Hammel, *Phys. Rev. E* **49**, 1140 (1994).
- [72] E. Ott and J. C. Sommerer, *Phys. Lett. A* **188**, 39 (1994).
- [73] P. W. Hammer, N. Platt, S. M. Hammel, J. F. Heagy, and B. D. Lee, *Phys. Rev. Lett.* **73**, 1095 (1994).
- [74] S. H. Strogatz, *Nonlinear Dynamics and Chaos* (Perseus, Philadelphia, PA, 1994).
- [75] R. Raynaud and E. Dormy, *Phys. Rev. E* **87**, 033011 (2013).
- [76] I. A. Belyaev, D. A. Biryukov, D. N. Gerasimov, and E. I. Yurin, *Chaos* **29**, 083119 (2019).
- [77] T. B. Hedley and J. F. Keffer, *J. Fluid Mech.* **64**, 625 (1974).
- [78] O. Terashima, Y. Sakai, K. Nagata, Y. Ito, K. Onishi, and Y. Shouji, *Exp. Therm. Fluid Sci.* **75**, 137 (2016).
- [79] D. J. Tritton, *Physical Fluid Science* (Oxford University, Oxford, 1988).
- [80] J. B. Gao, J. Hu, W. W. Tung, and Y. H. Cao, *Phys. Rev. E* **74**, 066204 (2006).
- [81] J. B. Gao, Y. H. Cao, W. W. Tung, and J. Hu, *Multiscale Analysis of Complex Time Series* (Wiley, New York, 2007).